nature portfolio

https://doi.org/10.1038/s41563-021-01066-4

Supplementary information

Effects of interlayer confinement and hydration on capacitive charge storage in birnessite

In the format provided by the authors and unedited

Supplementary Information

Effects of Interlayer Confinement and Hydration on Capacitive Charge Storage in Birnessite

Shelby Boyd,[1] Karthik Ganeshan,[2] Wan-Yu Tsai,[3] Tao Wu,[4] Saeed Saeed,[1] De-en Jiang,[4] Nina Balke,[5] Adri C.T. van Duin,[2] & Veronica Augustyn[1*]

[1] Department of Materials Science and Engineering, North Carolina State University, Raleigh NC 27606, USA

[2] Department of Mechanical Engineering, Pennsylvania State University, University Park PA 16803, USA

[3] Chemical Science Division, Oak Ridge National Laboratory, Oak Ridge, Tennessee 37830, USA

[4] Department of Chemistry, University of California, Riverside, CA 92521, USA

[5] Center for Nanophase Materials Sciences, Oak Ridge National Laboratory, Oak Ridge, Tennessee 37830, USA

[*] corresponding author's email: vaugust@ncsu.edu

I. Experimental Methods

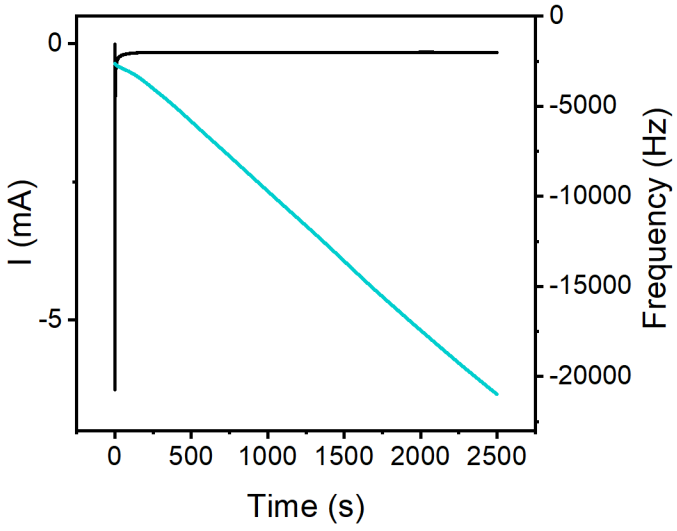

Figure S1. A typical birnessite electrodeposition monitored by EQCM, showing the chronoamperometric curve (black) and linear decrease in frequency change (blue), indicating a gain in mass.

A. EQCM Calibration

Although EQCM can be reliably used in liquid solutions,[1] the viscous loading on one side of the crystal requires re-calibration of the conversion factor for the Sauerbrey equation:

$$\Delta f = -C_f \Delta m \quad \text{(S1)}$$

In air, C_f = 56.6 Hz cm^2 μg^{-1}. The mass change in aqueous electrolytes was calibrated according to the protocol described in the SRS QCM200 manual and by Gabrielli et al.[1,2] Silver was deposited and stripped from an aqueous solution of 0.05 M $AgNO_3$ (Alfa Aesar) in 0.5 M HNO_3 (Fisher Scientific) onto a new crystal at 100, 200, 300, and 400 μA cm^{-2}, normalized to the overlapping area between the electrode on the back of the crystal and the active electrode on the front of the

crystal. The linear changes in frequency are shown in **Figure S2A**. We then used the following equation to calculate the equivalent C_f (in Hz/g) for each current density:

$$C_f = \frac{-F \times n \times \Delta f}{MW_{Ag} \times \Delta Q} \quad \text{(S2)}$$

Where: F = 96485 C mol^{-1} e$^-$

n = # of electrons transferred [mol e$^-$/mol Ag or other depositing species]

Δf = frequency change measured during deposition [Hz]

MW_{Ag} = molecular mass of silver [g/mol]

ΔQ = charge passed during deposition [C]

Plotting the four values of C_f *vs*. -log(i) (i = current density) gives **Figure S2B**. Here each value of C_f is clearly similar. To obtain the experimental C_f we averaged these values, and inverted that number, obtaining 24.42 ng Hz^{-1}. All EQCM frequency change data was multiplied by this number before background subtraction.

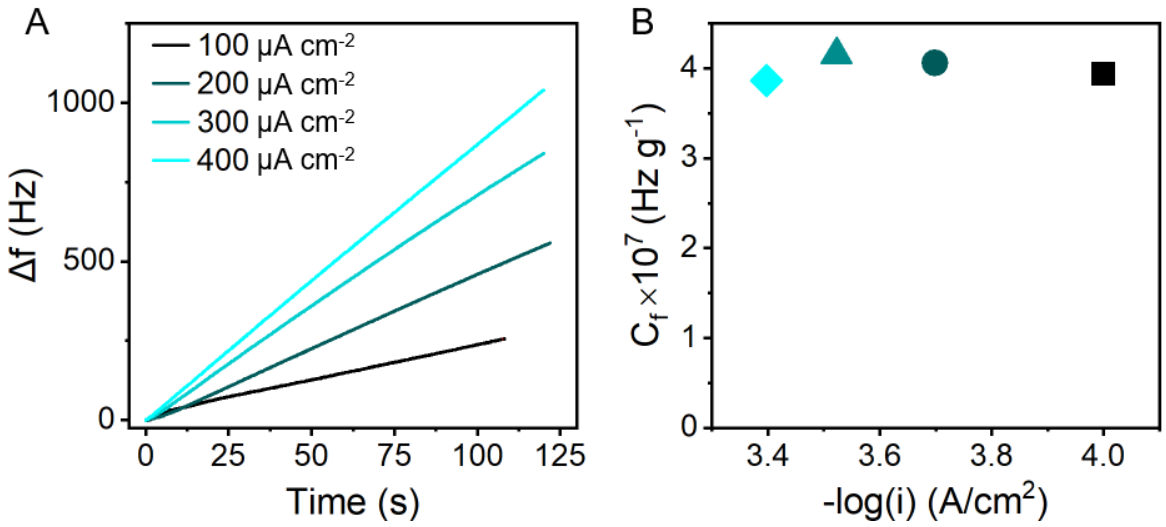

Figure S2. Data from the EQCM calibration in 0.5 M HNO_3 and 50 mM $AgNO_3$. **A)** The frequency change during Ag deposition. **B)** Calculated values of C_f at each current density, which were then averaged to obtain the experimental C_f.

Applicability of EQCM to Thin Films: In air, the change in frequency of the crystal used for EQCM was 7191 Hz, or 0.14% of the unloaded crystal's resonance frequency. This means that Sauerbrey's equation (S1) can be used to calculate the mass of the deposit,[1] which gives 180.3 μg (127 μg cm^{-2}). With a total charge passed during electrodeposition of 0.562 C, and assuming a 3 e^- reaction to reduce Mn^{7+} to Mn^{4+}, the molar mass of our electrodeposited film is 92.8 g mol^{-1}.[3] The mass of MnO_2 would be 86.9 g mol^{-1}, leaving ~5.9 g mol^{-1} unaccounted for. This can lead to a maximum of 0.15 mol K^+ with no interlayer water content, or 0.33 mol H_2O with no interlayer K^+ content. Since we expect both of these species to exist in the as-synthesized material, we propose the following composition: $K_{0.1}MnO_2 \cdot 0.1H_2O$.

When immersed in liquid, the unloaded crystal experiences a frequency drop of 640 Hz. Once birnessite is deposited, the film drops by 1047 Hz. Relative to the theoretical drop of 715 Hz for a polished crystal going from vacuum to liquid,[1] this is a reasonable change in frequency. We therefore confirm that this film is compatible with liquid-phase EQCM measurements.

B. ReaxFF Force Field Optimization and Validation using Density Functional Theory

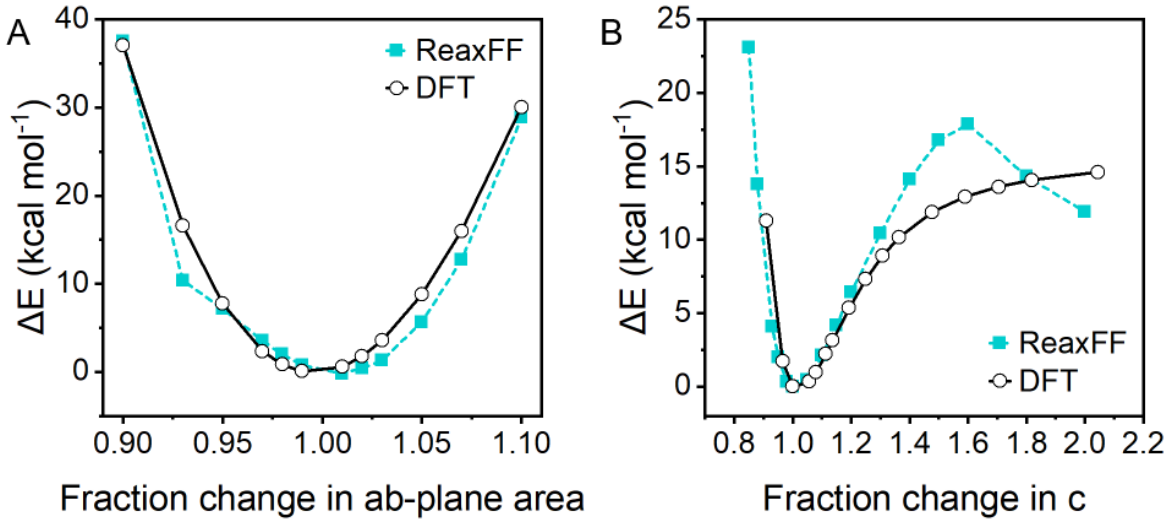

Figure S3. Comparison of ReaxFF and DFT-D3 energies for changes in (left) *ab*-plane area and (right) *c*-lattice length.

The DFT-D3 energies for the defects were calculated using VASP, using the procedure mentioned in the main text, with an energy cutoff of 520 eV and Monkhorst-Pack k-point mesh of 3×6×1. For the energy evaluation of K^+ intercalation, a gamma-centric k-point mesh of 2×2×2 was chosen with a convergence criterion of 0.05 eV/Å for forces. Table SI shows the binding energy of H^+ and water, and intercalation of K^+ in the MnO_2 layer.

Table SI. Comparison of DFT-D3 and ReaxFF energetics for species adsorption and intercalation in the MnO_2 layer(s).

Species	**Energy (kcal mol^{-1})**	
	ReaxFF	**DFT-D3**
H-binding MnO_2 surface	-79.41	-84.10
Water binding	-8.49	-3.70
$K_{0.125}MnO_2(H_2O)_{0.25}$ - $K_{0.0625}MnO_2(H_2O)_{0.25}$ - K	-144.86	-137.60

II. Supplementary Figures

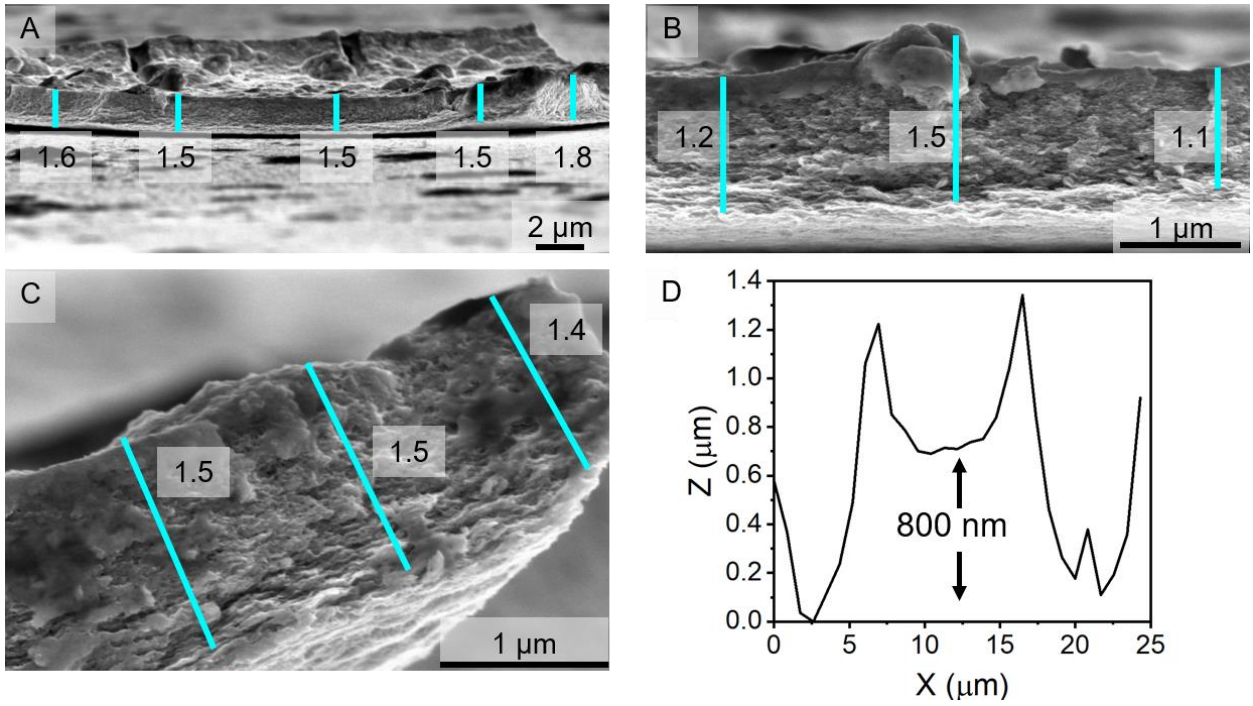

Figure S4. Film thickness calculated from A-C) SEM cross-sections and D) corroborated with AFM cross-sections. The SEM gives an average film thickness of 1.47 ±0.78 µm, and the AFM height trace across one of the islands shows an overall film thickness of 1-2 µm (1.4 µm in the spot shown), with raised edges and flatter island centers.

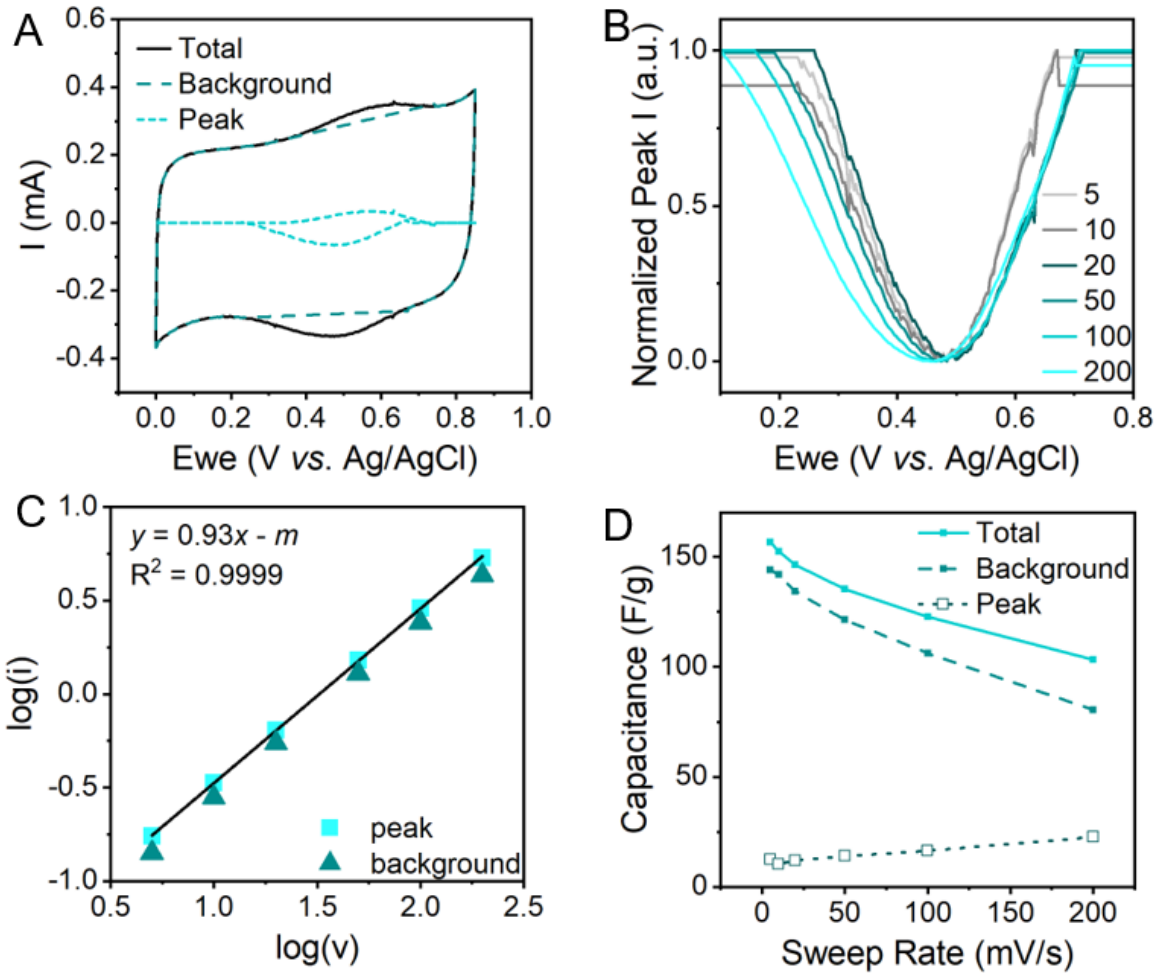

Figure S5. Deconvolution of the current contributions in cyclic voltammetry. A) CV of birnessite at 10 mV/s in 0.5 M K_2SO_4, showing the overall CV, the rectangular "background" current, and the isolated "peak" current. B) The normalized "peak" current at sweep rates from 5 – 200 mV/s, showing only slight polarization. C) Determination of the sweep rate dependence of the "background" and "peak" current. D) Separation of the total capacitance to the fractions originating from "background" and "peak" show that most of the capacitance is due to the "background."

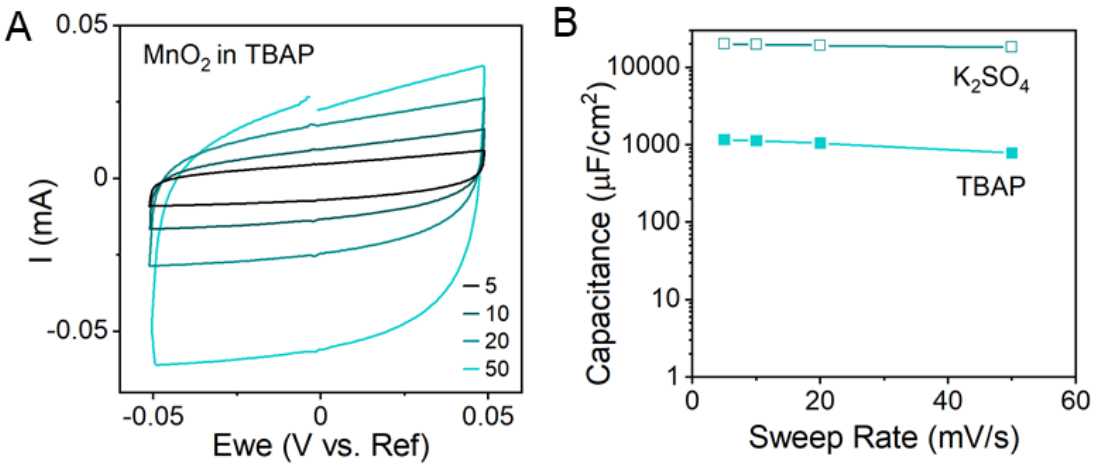

Figure S6. Quantification of the "outer surface" capacitance (not associated with cation intercalation) by cycling birnessite in a bulky cation aprotic electrolyte, 0.1 M tetrabutylammonium perchlorate (TBAP) in acetonitrile (ACN). A) CVs of a birnessite film in 0.1 M TBAP in ACN from 5 – 50 mV/s. B) Comparison of the capacitance (normalized to the geometric area) as a function of sweep rate for birnessite cycled in TBAP vs. K_2SO_4. At 5 mV s^{-1}, the capacitance in TBAP in ACN is 6.5% of the capacitance in aqueous K_2SO_4 electrolyte, indicating the minor contribution of the "outer surface" to the total capacitance.

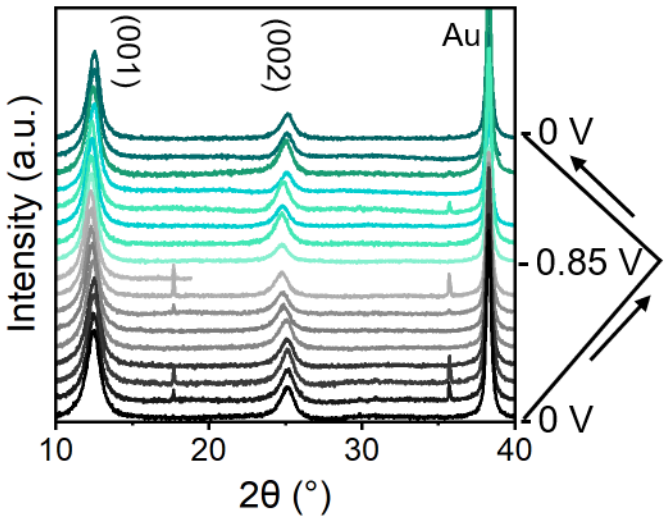

Figure S7. *Ex situ* XRD patterns from birnessite cycled between 0 and 0.85 V in 0.5 M K_2SO_4 electrolyte. Indexed peaks correspond to birnessite; unlabeled sharp peaks of lower intensity are due to residual salt from the electrolyte.

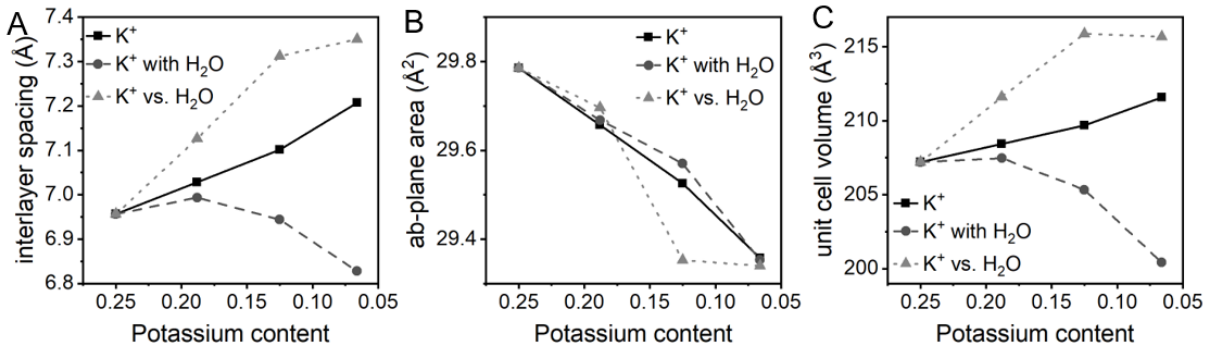

Figure S8. Unit cell parameters calculated from various DFT simulations for $K_xMnO_2{\cdot}yH_2O$ – $nK^+ \pm mH_2O$, where $m = 0$ or n. Values for m and n were chosen based on K^+ and H_2O contents common to birnessites. However, because the initial composition of our experimental samples is

unknown, these simulations represent overall trends. In particular, they are helpful to understand the structural changes observed via XRD and Raman.

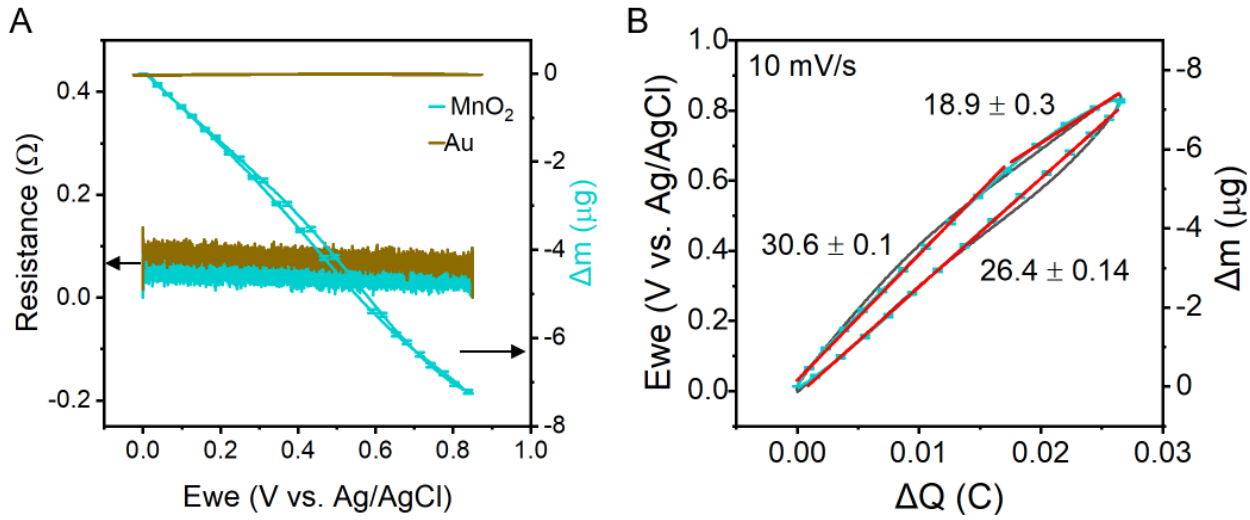

Figure S9. A) Resistance and change in mass of an electrodeposited birnessite film on a QCM crystal (MnO_2) and a bare QCM crystal (Au) as a function of applied potential at 10 mV/s in 0.5 M K_2SO_4. B) Plots of potential (black) and mass change (blue) vs. charge for birnessite cycled at 10 mV s^{-1} in 0.5 M K_2SO_4 and fitting of the results to two distinct anodic regions and one cathodic region (red) that could indicate related but slightly different processes involved in the charge storage mechanism. The first anodic region, with an MCR of ~ 30 g mol^{-1} e^- from 0 – 0.65 V, encompasses the area of the CV before and through the peak. The MCR indicates no change in charge storage mechanism at the inflection point in the mass change vs. potential curve ~ 0.3 V. This suggests that the same species are involved in the mechanism before and during the CV peak, but those removed early in the oxidation process may interact less strongly with the interlayer. After the peak in the CV, the MCR decreases to 19 g mol^{-1} e^- from ~ 0.65 – 0.85 V, the value expected for deintercalation of H_3O^+. The mass *vs*. potential and mass *vs*. charge graphs fail to

show a direct relation to each other during the cathodic cycle. During the cathodic cycle, the mass *vs*. potential curve in Figure 4A shows the reverse behavior of the anodic cycle, while the mass vs. charge graph (Figure S9) shows a single linear region with an MCR of 26 g mol^{-1} e^-.

Table S2. Mass-charge ratios of birnessite at different potential ranges from EQCM at 10 mV s^{-1}.

Potential Range (V)	**MCR (g/mol e^-)**	**e^-/mol MnO_2**
0 – 0.65	30.6 ± 0.1	0.09
0.63 – 0.85	18.9 ± 0.3	0.05
0.85 – 0	26.4 ± 0.02	0.14

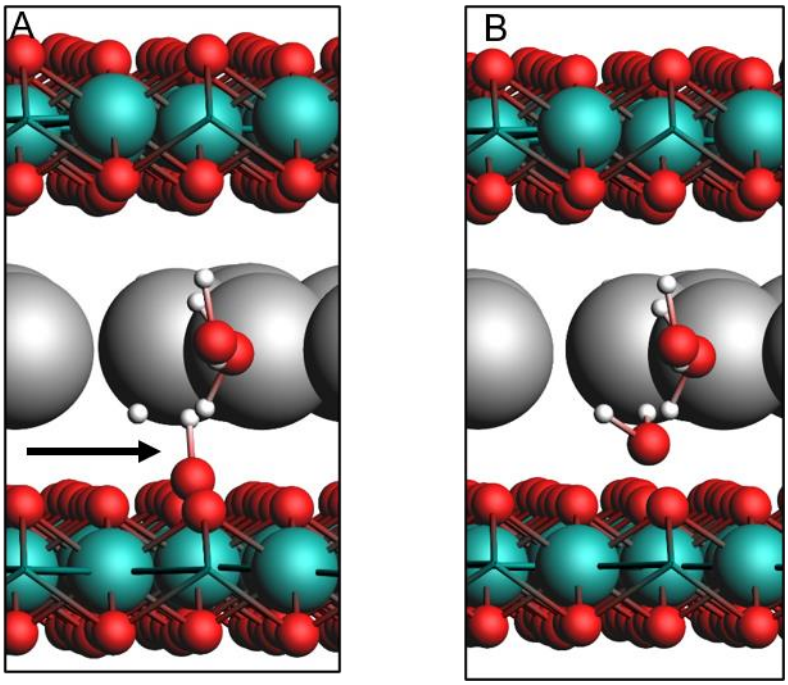

Figure S10. ReaxFF GCMC simulation of proton intercalation into birnessite. A) Protons are added to the O_{Mn} sites on the surface close to water molecules, in regions with lesser K^+ interference. B) This favors the subsequent reduction of the oxygen forming a vacancy (*) of the type MnO(*) and molecular water with H_2O_{Mn} at the surface, similar to that seen in hydrated $H_2Ti_3O_7$ structures.[4]

The chemical potential of H^+ was obtained by averaging the potential energy of a single proton in 520 water molecules under NVT-ensemble MD simulation to mimic the effects of high pH. It must be noted that the current force field is not explicitly trained for the vacancy formation mechanism. Therefore, further studies may be necessary to determine the extent of this effect.

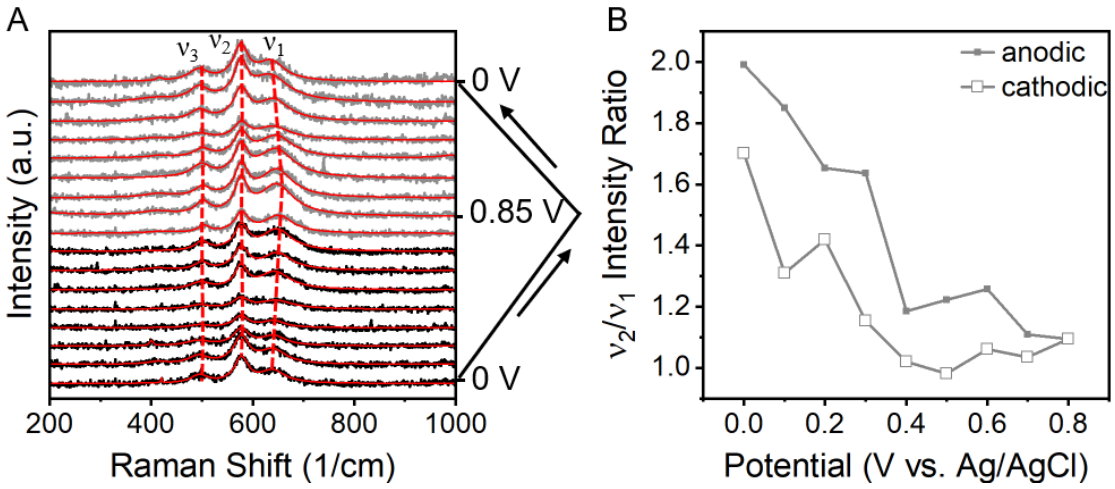

Figure S11. A) *In situ* Raman spectra of birnessite MnO_2 during electrochemical cycling in 0.5 M K_2SO_4. The thin red lines represent the result of peak fitting. Only the v_1 peak changes appreciably with potential. B) Comparison of the intensity of the v_1 to v_2 Raman peaks as a function of potential during K^+ de/intercalation. Both the ν_1 and ν_2 peaks are sensitive to the interlayer environment, with the v_1 peak center increasing in wavenumber and intensity with oxidation, while the wavenumber of the v_2 peak decreases.[5–8]

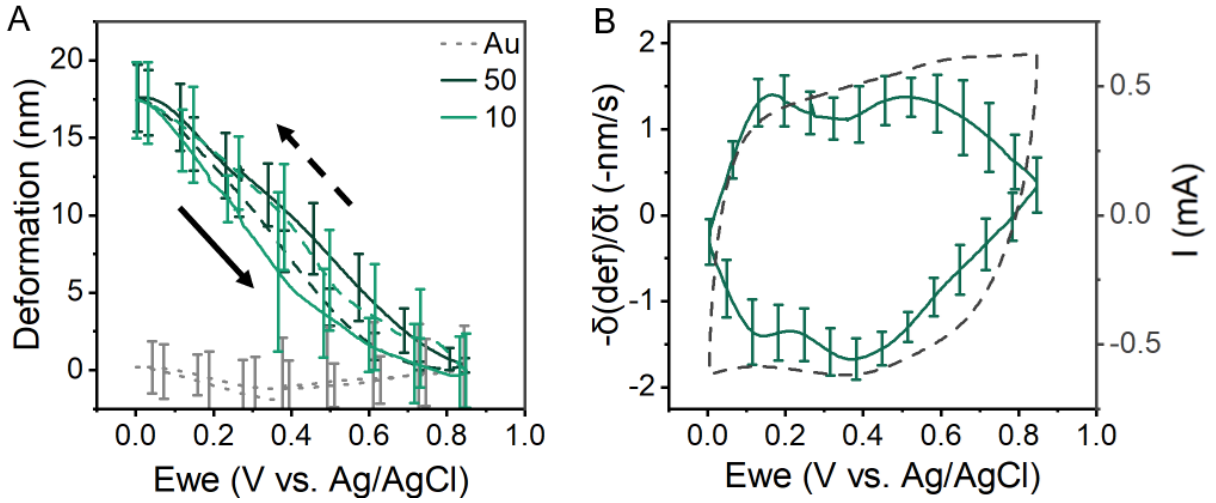

Figure S12. *Operando* AFM dilatometry of birnessite on the points shown in Figure 2F in 0.5 M K_2SO_4. **A)** Potential-dependent deformation at 10 and 50 mV s^{-1}. The deformation curves of birnessite at both rates almost entirely overlap, indicating the same charge storage mechanisms. The gold background at 50 mV s^{-1} ("Au") shows no deformation, as expected for a material that does not undergo any volume change over this potential range. **B)** mCV at 50 mV s^{-1} from *operando* AFM dilatometry shows two sets of reversible deformation rate peaks during electrochemical cycling

At both rates the deformation is the same despite the additional noise from thermal drift at 10 mV s^{-1}. The measurements performed on gold electrodes show that the signal originates from volume changes of birnessite, and not electrostatic electrode-tip interactions. The film contracts with oxidation, contradicting the interlayer spacing changes shown by XRD, Raman, and DFT unit cell calculations. Based on the SEM images (**Figure 2** and Figure S4), we propose that the AFM response represents primarily the deformation associated with the *ab*-plane of birnessite rather than along the *c*-axis. The area of the *ab*-plane (**Figure S8**) is predicted to decrease regardless of

the intercalation mechanism. Previous *operando* diffraction studies show that the increase in interlayer spacing upon oxidation is accompanied by a decrease in the *a* and *b* lattice parameters, leading to an overall ~ 0.5% decrease in unit cell volume.[9,10] The DFT calculations (Figure S8) predict a unit cell expansion for K^+ de-intercalation and K^+ de-intercalation coupled to H_2O intercalation, and a unit cell contraction for K^+ and H_2O de-intercalation. However, the unit cell volume only decreases for the scenario in which both K^+ and H_2O de-intercalate, which contradicts the mechanism suggested by EQCM.

Rate-dependence of AFM and EQCM data

Having shown that birnessite stores charge via interlayer processes, we now consider the effect of sweep rate. **Figure S13** shows the rate-dependent deformation and mass change of birnessite. The deformation exhibits slight decrease with rate in K_2SO_4, maintaining 75% of its 17.6 nm deformation at 200 mV s^{-1}. Capacitance and mass change retention are 71% and 84% of the 158 F g^{-1} and 7.23 μg at 10 mV s^{-1}, respectively.

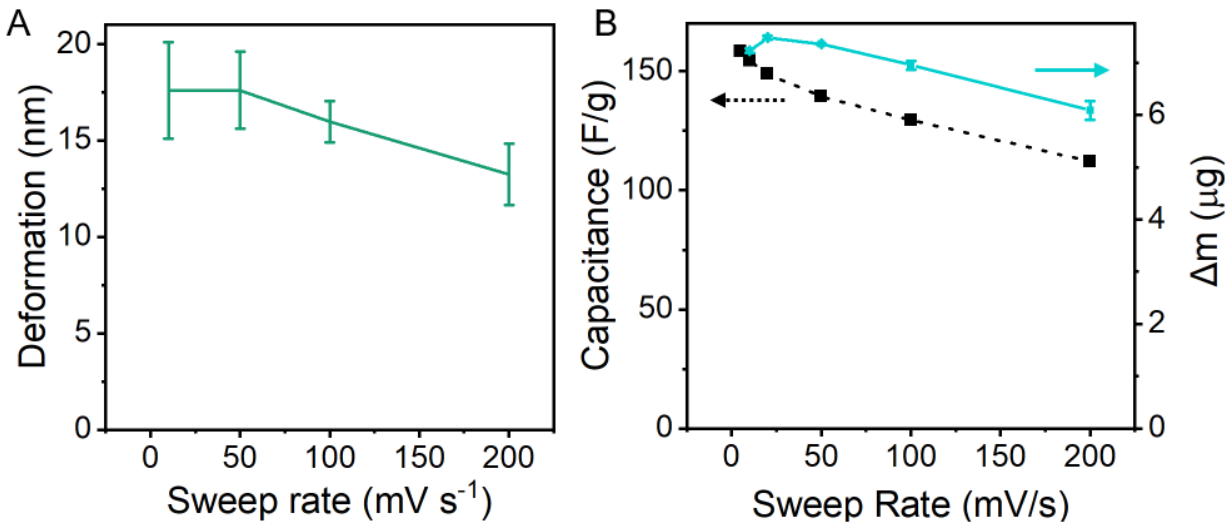

Figure S13. Rate behavior of birnessite during *operando* AFM and EQCM. A) Deformation from 50 – 200 mV s^{-1} in K_2SO_4. B) Mass and capacity changes from 10 – 200 mV s^{-1}.

Figure S14 shows the rate-dependent CVs, mCVs, gCVs and MCRs of birnessite MnO_2. There are two sets of peaks in the mCV (Fig. 13B), supporting our earlier claim that the AFM can detect processes not visible in global measurement techniques, and that there may be multiple processes occurring in the K_2SO_4 electrolyte. In Figure 10C the overall shape of both gCV and CVs remains the same, showing increasing polarization with sweep rate. The polarization at higher

rates is to be expected, as the relatively low conductivity of birnessite MnO_2 and the ~2D ion diffusion through the longer dimensions of the nanosheets leads to some polarization and delay of interlayer redox at higher rates.[11] Overall, the interlayer water does appear to improve the structural integrity and rate capability of birnessite MnO_2. However, if an opposing water flux is critical to the good pseudocapacitive performance of birnessite MnO_2 in K_2SO_4, the reduced water exchange with K^+ may lead to reduced room for K^+ in the interlayer and therefore reduced capacitance. These data do show that the charge-storage in birnessite is still due to interlayer mechanisms.

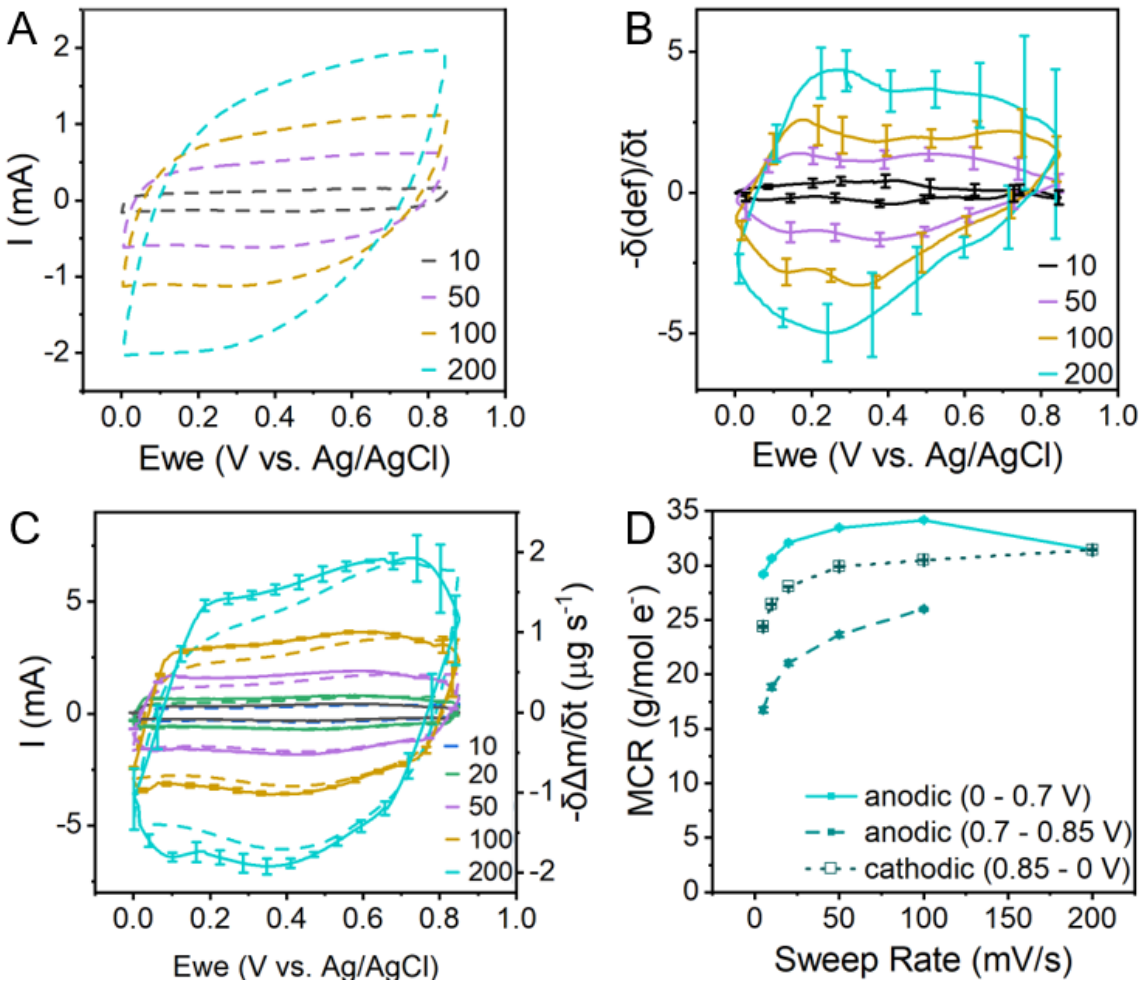

Figure S14. Electrochemomechanical and gravimetric behavior of birnessite as a function of rate. A) CVs from *operando* AFM show some polarization but maintain their shape from 10 to 200 mV s^{-1}. B) The mCVs show two sets of peaks, maintaining the behavior observed at 50 mV/s. C) The CVs and gCVs match, suggesting that interlayer behavior remains dominant. D) MCRs slowly increase with sweep rate. If the species involved in the intercalation mechanism are K^+ and H_2O, this may indicate that there is less opposing H_2O flux with increasing sweep rates.

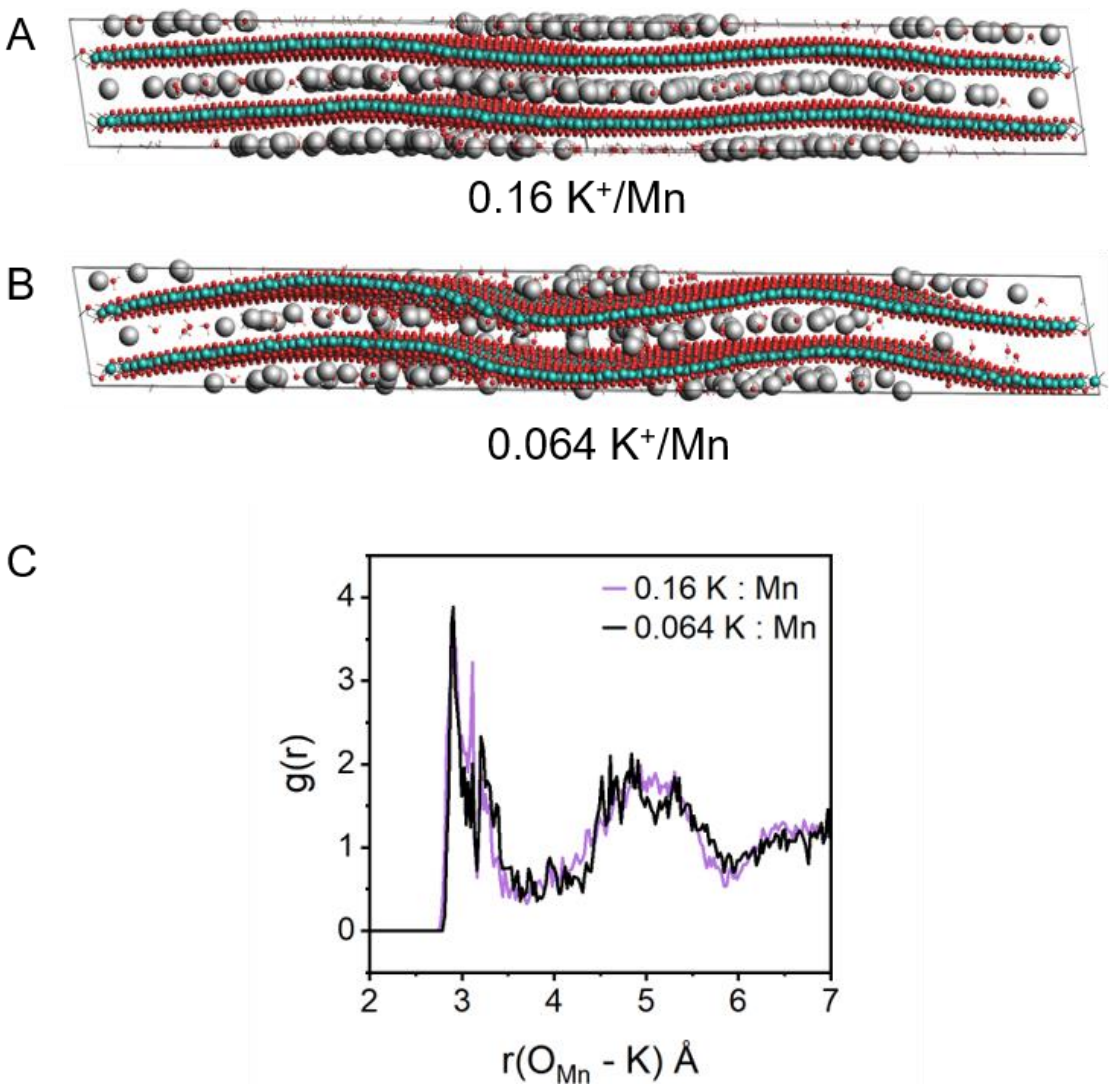

Figure S15. Effect of inhomogeneity in the cation distribution in the interlayer. A) The system with a more filled interlayer (0.16 K^+/Mn) shows less significant wrinkling than the sparsely filled system in B) with 0.064 K^+/Mn (reproduced for the sake of comparison from Figure 8A). C) Radial distribution function of K^+ and O_{Mn} indicating no substantial change in K^+-O_{Mn} distance between the two systems, with the first peak being close to 3 Å.

Note: This result does not indicate that MnO_2 is more flexible in the absence of K^+ but suggests that the local inhomogeneity in the distribution of K^+ promotes the large-scale distortions seen in

the layer. As seen in Movie S1, we indeed find that the presence of intercalants – especially K^+ – is vital in developing the distortions.

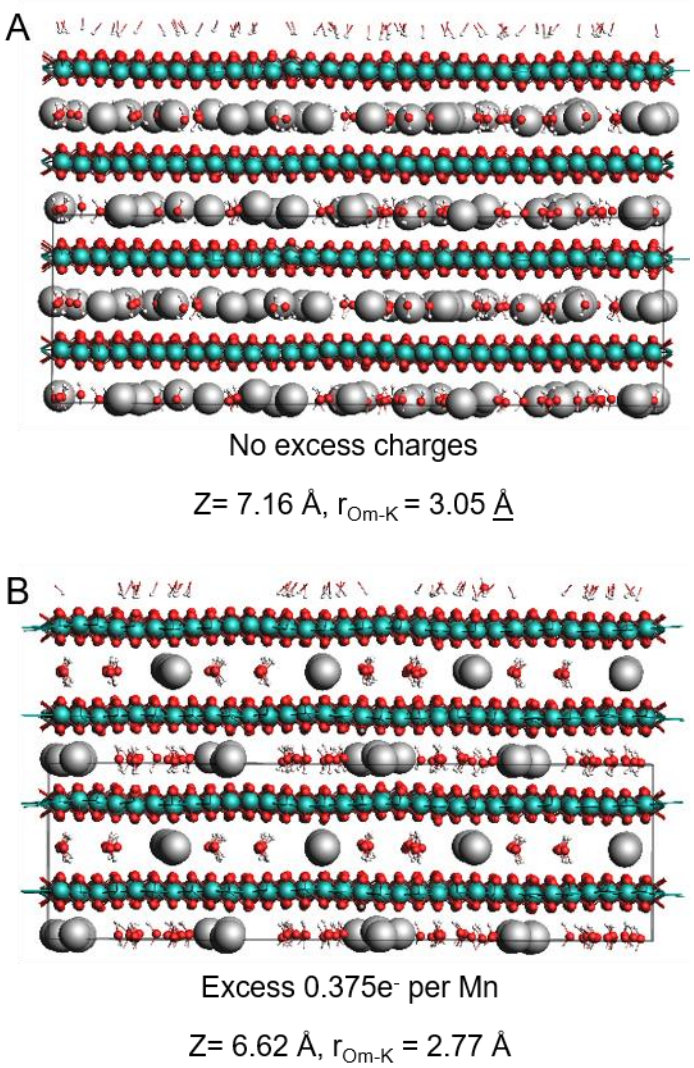

Figure S16. Snapshots from the NPT-MD simulation with stratified charges. A) With no charge stratification, the K^+-O_{Mn} distance is close to 3 Å with the interlayer spacing of 7.16 Å. B) With high charge stratification of 0.375e^-/Mn, the interlayer spacing decreases to 6.62 Å while the K^+-O_{Mn} distance reduces to 2.77 Å.

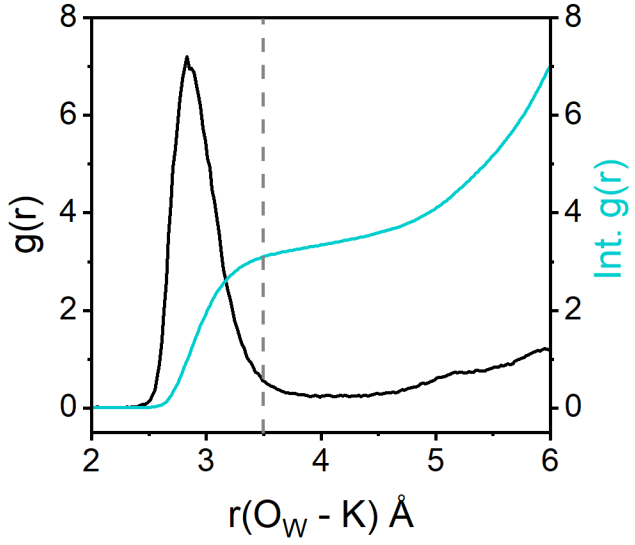

Figure S17. Solvation of K^+ in the nanoconfined and hydrated interlayer of birnessite. RDF of K^+ and water oxygen O_{Mn} (left axis), and the integral of g(r) (right axis) indicating the coordination number of K^+ by neighboring interlayer water molecules. The trajectory for the evaluation of the coordination number was obtained using an NVT-MD simulation of the final GCMC structure described in Figure 4C and Movie S1. With a coordination number of ~3.2 at 3.5 Å, we conclude that K^+ loses at least half of its solvation shell upon intercalation in comparison to bulk electrolyte.

References

(1.) Stanford Research Systems. *Operation and Service Manual QCM200 Quartz Crystal Microbalance Digital Controller QCM25 5 MHz Crystal Oscillator*; **2016**.

(2.) Gabrielli, C.; Keddam, M.; Torresi, R. Calibration of the Electrochemical Quartz Crystal Microbalance. *J. Electrochem. Soc.* **1991**, 138, 2657.

(3.) Shamoto, M.; Tanimoto, T.; Tomono, K.; Nakayama, M. EQCM Investigation on Electrodeposition and Charge Storage Behavior of Birnessite-Type MnO_2. *ECS Trans.* **2013**, 50, 85–92.

(4.) Fleischmann, S.; Sun, Y.; Osti, N. C.; Wang, R.; Mamontov, E.; Jiang, D.-E.; Augustyn, V. Interlayer Separation in Hydrogen Titanates Enables Electrochemical Proton Intercalation. *J. Mater. Chem. A.* **2020**, 8, 412-421.

(5.) Chen, D.; Ding, D.; Li, X.; Waller, G. H.; Xiong, X.; El-Sayed, M. A.; Liu, M. Probing the Charge Storage Mechanism of a Pseudocapacitive MnO_2 Electrode Using in Operando Raman Spectroscopy. *Chem. Mater.* **2015**, 27, 6608–6619.

(6.) Yang, L.; Cheng, S.; Wang, J.; Ji, X.; Jiang, Y.; Yao, M.; Wu, P.; Wang, M.; Zhou, J.; Liu, M. Investigation into the Origin of High Stability of δ-MnO_2 Pseudo-Capacitive Electrode Using Operando Raman Spectroscopy. *Nano Energy* **2016**.

(7.) Julien, C.; Massot, M.; Baddour-Hadjean, R.; Franger, S.; Bach, S.; Pereira-Ramos, J. P. Raman Spectra of Birnessite Manganese Dioxides. *Solid State Ionics* **2003**, 159, 345–356.

(8.) Hsu, Y. K.; Chen, Y. C.; Lin, Y. G.; Chen, L. C.; Chen, K. H. Reversible Phase Transformation of MnO_2 Nanosheets in an Electrochemical Capacitor Investigated by in

Situ Raman Spectroscopy. *Chem. Commun.* **2011**, 47, 1252–1254.

(9.) Shan, X.; Guo, F.; Page, K.; Neuefeind, J. C.; Ravel, B.; Abeykoon, A. M. M.; Kwon, G.; Olds, D.; Su, D.; Teng, X. Framework Doping of Ni Enhances Pseudocapacitive Na-Ion Storage of (Ni)MnO_2 Layered Birnessite. *Chem. Mater* **2019**, 31, 8786.

(10.) Shan, X.; Guo, F.; Charles, D. S.; Lebens-Higgins, Z.; Abdel Razek, S.; Wu, J.; Xu, W.; Yang, W.; Page, K. L.; Neuefeind, J. C.; Feygenson, M.; Piper, L. F. J.; Teng, X. Structural Water and Disordered Structure Promote Aqueous Sodium-Ion Energy Storage in Sodium-Birnessite. *Nat. Commun.* **2019**, 10, 4975.

(11.) Wang, W.; Juarez-Robles, D.; Mukherjee, P. P. Electroanalytical Quantification of Electrolyte Transport Resistance in Porous Electrodes. *J. Electrochem. Soc.* **2020**, 167, 080510.